

Towards Finding Energy Efficient Paths for Hybrid Airships in the Atmosphere of Venus

Bernardo Martinez R. Jr., Anna Puigvert I Juan, and Guilherme A. S. Pereira

Abstract—This paper presents a solution to the motion planning problem for an autonomous airship under super-rotation winds of the Venusian atmosphere. The airship uses both buoyancy and aerodynamic lift to control its altitude. In addition, solar panels distributed over the aircraft provide energy to the propellers and allow for battery recharging. Our approach uses a sampling-based planner that relies on Dubins’ Airplane paths deformed under the influence of the winds to create a tree of kinematically feasible trajectories. We use the battery state to prune energetically unfeasible trajectories and we propose a cost function that accounts for the energy expenditure of the propulsive system and that considers battery charging by using the Economics notion of opportunity cost. The method is illustrated through a series of simulations that show how the vehicle takes longer and high-altitude paths to minimize the use of energy and favor battery recharge. Our results also show that naive trajectories are not feasible in terms of energy, justifying the need for more efficient solutions.

I. INTRODUCTION

Venus has been considered Earth’s twin planet due to its similar composition, mass, gravitation, and radius. Researchers believe that Venus may have had a shallow ocean and livable surface conditions during 2 billion years of its early existence. However, past exploration missions found that, today, at the surface of Venus, the environment is hugely different from Earth, with temperatures exceeding 450°C and atmospheric pressure more than 90 times larger than Earth’s [1]. Venus went through a transformation due to the greenhouse effect, being 96% of its current atmosphere composed of carbon dioxide [2]. Understanding what happened to Venus in the past can give insight into what can happen on Earth in the future, as greenhouse gases accumulate in our atmosphere.

While exploring the Venusian surface is extremely hard, its atmosphere has air pressure, temperature and density comparable to what is found on Earth. From 50 to 70 km altitude, the pressure ranges from 1.066 to 0.0369 bar, the temperatures from 76.85 to -43.15°C , and the air density from 1.594 to 0.084 km/m^3 [3]. Conceptual vehicle designs have been proposed for exploring Venus [4]. Some of these concepts are autonomous fixed-wing solar-powered aircrafts [5], [6], [7], including semi-buoyant inflatable planes,

This research was made possible with support from the NASA Established Program to Stimulate Competitive Research, Grant #WV-80NSSC21M0145, and the Benjamin M. Statler Fellowship.

Authors are with Mechanical and Aerospace Department at Benjamin M. Statler College of Engineering and Mineral Resources, West Virginia University, Morgantown, WV, 26501 USA.

Emails: bm00002@mix.wvu.edu, ap00063@mix.wvu.edu, guilherme.pereira@mail.wvu.edu

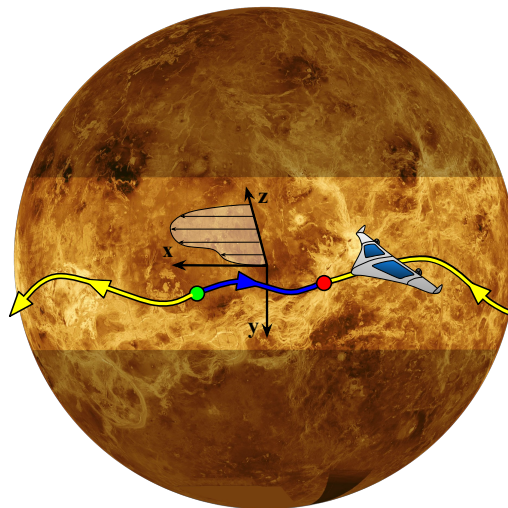


Fig. 1: The solution of a motion planning problem in the atmosphere of Venus can result in the most efficient path to a desired goal being very different from the shortest path when considering the vehicle dynamic constraints and environmental properties such as high-speed winds and available solar power. In the figure, green and red dots represent start and goal region, respectively. The yellow path is more energetically efficient than the blue path, which is shorter. The thin arrows represent magnitude and direction of the wind field.

also know as hybrid airships [8], which are the focus of this paper.

Even with reasonable climate conditions, the atmosphere of Venus still imposes challenges to a fixed-wing aircraft. It has, for example, high-speed zonal winds, called super-rotation winds [9], that can reach speeds greater than 100 m/s . As a consequence, a vehicle left to drift in the atmosphere will circle the planet in as few as four Earth-days and, unless the vehicle is powerful enough to counteract these wind speeds, it is expected that it will experience long periods in the absence of light, making them dependent on charged batteries for controlled flight during these periods [10]. These challenges raise the problem of how to obtain the optimal path that these aircrafts should follow. As illustrated in Fig. 1, in such an environment, the energy optimal path may be very different than the shortest path.

We want to design motion planners that: 1) create minimum energy paths, since the vehicles have limited battery and will fly for long periods of time; 2) account for battery re-charging; and 3) account for the strong winds in which

the aircraft will fly. Several previous works have solved some of these problems on Earth [11], [12], [13], [14], [15]. A real-time environment-aware planner has been proposed in [11] using variations of RRT* [16], that approximate the dynamics of the aircraft using Dubins' Airplane [12], and incorporating wind field data in its heuristics. A minimum energy planner was proposed in [13] for a UAV subject to wind caused by urban canyons. The authors used a A* grid search to find a minimum cost path, and their proposed cost function is based on the change of total energy: composed by potential, kinetic, and stored energy (battery). However, their model assumed constant altitude, constant airspeed and no recharging. Consequently, the total energy decreases monotonically with the consumption of the stored energy. Also, their method require wind speeds to be smaller than the airspeed to converge. Path planners for a gliding aircraft under complex wind fields were studied in [14], [15]. These planners grow a tree of feasible trajectories from a discrete set of allowable inputs and weigh the branches using a cost function that accounts for changes in total energy and distance to the goal. Further, this method allows for increase of potential energy caused by the vertical component of wind, what is known as static soaring.

In this work, we present a sampling-based path planner for a fixed-wing, hybrid airship that relies on Dubins' Airplane as a local planner and accounts for the influence of strong winds. The planner optimizes a cost function based on energetic transactions. This cost function includes not only expenditure, in the form of thrust or drag, but also accumulation, in the form of charging using solar panels and gains in potential energy (e.g., with upward directional winds). It is important to mention that the naive inclusion of such influx energy could generate negative costs for some paths, what would violate the requirements for most optimizers [16]. We then, use the notion of *opportunity cost* [17], the loss of gain caused by choosing not to follow an alternative that can offer the highest benefit. In our case, when considering solar power, the cost is computed as the difference between the maximum charging energy that the vehicle could gain (e.g., when flying above the clouds) and the energy gained when it is flying in a less favorable altitude. Therefore, the main contributions of this paper are:

- An energy efficient sampling-based motion planning strategy that i) uses wind-deformed Dubins' Airplane trajectories as local planners, ii) includes a semi-buoyant dynamic model for the aircraft, iii) accounts for the vehicle's battery state.
- A cost function that i) accounts for the energy expenditure of the propulsive system and ii) considers battery charging as an opportunity cost, thus avoiding negative costs in the function.

This paper is organized as follows. Problem definition is presented in Sect. II. Our motion planning approach is explained in details in Sect. III. Some numerical results are presented in Sect. IV. Finally, conclusions and future work are presented in Sect. V.

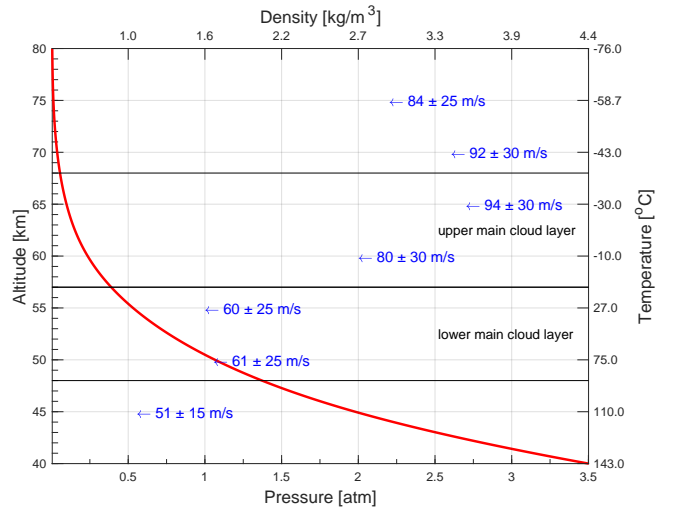


Fig. 2: Atmospheric characteristics of Venus. Wind is illustrated by the blue left arrows where each value represents the average wind speed and its possible variation in function of the altitude.

II. PROBLEM DEFINITION

This section describes the problem we are dealing with in this paper, especially the environment and the airship. We show the equations necessary to describe the force equilibrium during the flight of the aircraft and its dynamic and kinematic models.

A. The environment

In this work we target a region of the atmosphere of Venus within 50 km to 70 km altitude, where exploration is viable. For this region, atmospheric properties as temperature, $\Theta(z)$, pressure, $p(z)$, air density, $\rho(z)$, and wind field, $w(x, y, z)$, where x and y represent latitude and longitude respectively and z represents the altitude, were obtained from data tables presented in [3], compiled from data of several past missions to Venus [2]. The gravitational acceleration, $g(z)$, is approximately 8.87 m/s^2 , changing only slightly with the altitude. For simplicity, all properties are assumed to be time-invariant. We assume that the wind field is dominated by the super-rotation winds, which is compatible with the observations near the equatorial region [9]. Fig. 2 shows the density, temperature and pressure in relation to the altitude. Wind and cloud layers are also displayed according to the altitude. The farther we get from the Venusian surface, the lower density, temperature, and pressure we get. Wind speeds vary from around $61 \pm 25 \text{ m/s}$ at 50 km altitude to $92 \pm 30 \text{ m/s}$ at 70 km altitude.

Another factor considered in our model is the availability of solar intensity ($I_{solar}(z)$) to charge the batteries and power the aircraft. Venus is exposed to a solar flux of 2600 W/m^2 (this is also called exoatmospheric solar flux), almost double the solar flux that Earth is exposed to. However, this flux is attenuated by the atmosphere. The available solar intensity (ratio between available flux and the exoatmospheric) is 95% at the top of the clouds (at 65 km altitude) and 20 to 50% at

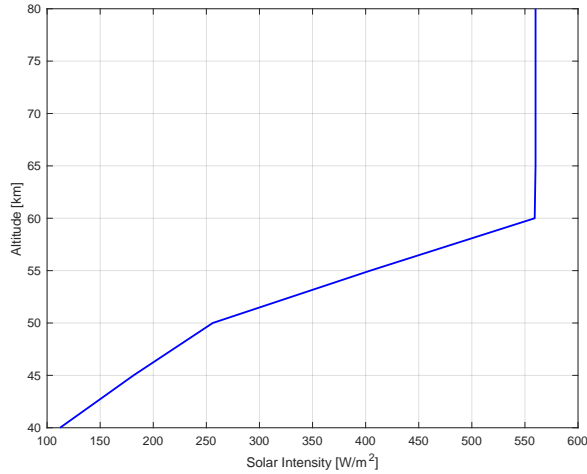


Fig. 3: Venus solar intensity with respect to altitude. The graph also considers the conversion efficiency of the solar panels.

TABLE I: Vehicle Design Parameters

Parameters	Values	Parameters	Values
Aircraft Mass	450 kg	Solar Panel Area	50 m ²
Aircraft Volume	490 m ³	Battery Max. Energy	50 MJ
Wing Span	50 m	Propellers Efficiency	0.8
Mean Aerodynamic Chord	10 m	Shaft Efficiency	0.8
Wing Area	500 m ²	Airspeed Limits	0-30 m/s
Wing Aspect Ratio	5	Roll Angle Limits	±30°
Oswald Efficiency Number	0.85	Flight Path Angle Limits	±45°
Zero-lift Drag Coeff.	0.02		

the bottom of the cloud layer (at 40 km altitude), depending on the considered wavelength. Further, solar panels have an intrinsic efficiency in converting solar power to stored energy in the batteries. A model for the solar intensity in Venus considering this energy conversion efficiency was obtained from [10] and is shown in Fig. 3.

B. The vehicle

In this work we are considering a vehicle based on the concept proposed by [8]. This vehicle is a semi-buoyant unmanned propelled aircraft. To provide buoyancy, the aircraft has a light-weight design and is filled with a low density gas. At 70 km above Venus surface, the vehicle is expected to be 10% buoyant with 90% lift from the propellers. At low altitudes the vehicle is 100% buoyant. The aircraft is solar-powered and its solar panels are distributed over its body. The maximum airspeed of the vehicle is 30 m/s. Table I shows the main design parameters used in this paper.

C. Aircraft Steady Flight and Kinematic Models

The hypothesis for our work is that the aircraft is able of two coordinated flight modes. Given a desired flight path angle, the first mode is flying in a straight line and the second is turning with a constant bank angle, both with respect to the wind reference frame. Similarly to what is proposed in [14], we consider that switching between steady turn and steady climb/descent is fast compared to the duration of the command itself and that a point-mass model is sufficient

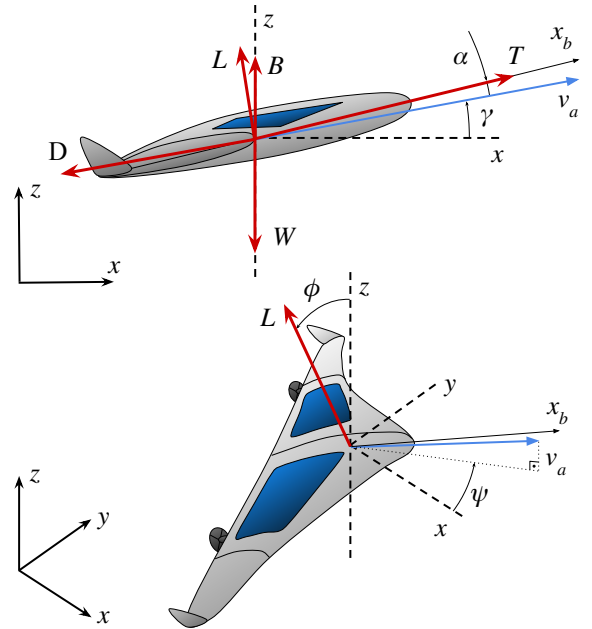


Fig. 4: Coordinate frames and free-body diagram of the vehicle. The flight path, heading, and roll angles (γ , ψ , ϕ) are given with respect to the inertial frame (x , y , z). The thrust force is assumed to be aligned with x -axis of the vehicle's body frame, which is denoted by x_b .

to represent the vehicle. Further, for this work, we assume that the aircraft maintains its airspeed constant. Fig. 4 shows a free-body diagram of a point-mass model of the aircraft where W is the weight of the aircraft, B is the buoyancy force, L is the lift force, D is the drag force, T is the thrust force, α is the angle of attack of the aircraft with respect to the airflow (represented by v_a), γ is the flight path angle, ψ is the heading angle, and ϕ is the roll angle.

For our planning purposes, we need to obtain an expression for the thrust required at any given point of the aircraft trajectory. By equating the forces parallel and perpendicular to the vehicle airspeed we have

$$(W - B) \cos \gamma = L \cos \phi + T \sin \alpha \quad (1)$$

$$(W - B) \sin \gamma = D - T \cos \alpha. \quad (2)$$

The term $(W - B)$ can also be written as $(m - \rho V)g$, where m is the mass of the aircraft, ρ is the density of the fluid, V is volume of the aircraft, and g is the acceleration of gravity. Both density and gravity are variable with the altitude of the vehicle. Considering that the angle of attack is usually small, we assume the approximations $T \sin \alpha \approx 0$ and $T \cos \alpha \approx T$. Given a specific input $\mathbf{u} = [v_a, \gamma, \phi]^T$ and the wing area (S), we can rewrite (1) and obtain the lift force and lift coefficient as

$$L = \frac{(m - \rho V)g \cos \gamma}{\cos \phi} \Rightarrow c_L = \frac{L}{\frac{1}{2}\rho v_a^2 S}. \quad (3)$$

We represent the drag coefficient with a second-order polynomial using the lift coefficient, the wing aspect ratio (\mathcal{R}), and the Oswald efficiency number (e). This allow us

to calculate the drag force exerted on the vehicle:

$$c_D = \sum_{i=0}^N a_i c_L^i = c_{D,0} + \frac{c_L^2}{\pi R e} \Rightarrow D = \frac{1}{2} \rho v_a^2 S c_D. \quad (4)$$

Finally, by rewriting (2) and including our model for the drag force from (4), we obtain the required thrust as

$$\begin{aligned} T &= D - (W - B) \sin \gamma \Leftrightarrow \\ T &= \frac{1}{2} \rho v_a^2 S c_D - (m - \rho V) g \sin \gamma. \end{aligned} \quad (5)$$

Additionally to the balance of forces, the kinematic model for the aircraft motion under the influence of the wind presented in [14] is extended to account for the buoyancy of the vehicle:

$$\begin{aligned} \dot{x} &= v_a \cos \gamma \cos \psi + w_x \\ \dot{y} &= v_a \cos \gamma \sin \psi + w_y \\ \dot{z} &= v_a \sin \gamma + w_z \\ \dot{\psi} &= \frac{(m - \rho V) g \cos \gamma \tan \phi}{m v_a}. \end{aligned} \quad (6)$$

where $\dot{\psi}$ is obtained from $L \sin \phi = m v_a \dot{\psi}$.

D. Motion Planning Problem

The position of the aircraft is given by $\mathbf{p} = [x, y, z]^T$, where x , y and z represent, respectively, the Cartesian coordinates aligned with longitude, latitude and altitude, and the heading angle is given by ψ . The configuration vector is then given by $\mathbf{x} = [x, y, z, \psi]^T$. We also keep a separate state, b , to account for the battery level of the vehicle. The input vector $\mathbf{u} = [v_a, \gamma, \phi]^T$ includes the airspeed, v_a , flight path angle, γ , and roll angle, ϕ , of the vehicle. The wind field experienced by the aircraft $\mathbf{w} = [w_x, w_y, w_z]^T$ will vary with its position, as it moves through the wind field.

Our goal is to find a feasible and low-energy path that guides a hybrid airship from the initial configuration \mathbf{x}_{start} to the final configuration \mathbf{x}_{goal} in a finite time, subject to the dynamic equations given by $\dot{\mathbf{x}} = f(\mathbf{x}, \mathbf{u}, \mathbf{w})$ and respecting the constraints in the configuration and input spaces.

III. METHODOLOGY

Our sampling algorithm, inspired by RRT* [18], builds and maintains a tree graph $\tau(V, E)$ using a set of vertices, V , and a set of edges, E . The algorithm samples a random point in the configuration space, finds its nearest vertex in the current tree, uses an approximated steering function to create a vertex based on the random point and its nearest vertex, and, finally, selects the actual parent for this vertex using a more appropriated steering function that also returns the cost of the path between a vertex and its potential parent. One important difference from other similar methods like [11] is that, since we are not considering an environment with obstacles, we do not have strict requirement for the path and the vertices that are going to be added to the tree. Therefore, instead of forcing the aircraft to reach the selected vertex, we allow the wind to deform the trajectory created when connecting a new vertex and its potential parents. Differently

Algorithm 1 Energy-efficient and wind-aware RRT planner

```

function  $\tau = \text{EW-RRT}(\mathbf{x}_{start}, \mathbf{x}_{goal}, d, d_{min})$ 
   $v_{init}, v_{goal} \leftarrow \mathbf{x}_{start}, \mathbf{x}_{goal}$ 
   $\tau \leftarrow \text{InitializeTree}()$ 
   $\tau \leftarrow \text{InsertNode}(\tau, \emptyset, v_{init})$ 
  for  $i \leftarrow 1, N$  do
     $v_{rand} \leftarrow \text{Sample}()$ 
     $v_{nearest} \leftarrow \text{Nearest}(\tau, v_{new})$ 
     $v_{new} \leftarrow \text{ApproxSteer}(v_{nearest}, v_{rand}, d)$ 
     $V_{near} \leftarrow \text{Near}(\tau, v_{new})$ 
     $v_{min}, v_{new} \leftarrow \text{BestParent}(V_{near}, v_{nearest}, v_{new})$ 
     $\tau \leftarrow \text{InsertNode}(\tau, v_{min}, v_{new})$ 
    if  $\text{Distance}(v_{new}, v_{goal}) < d_{min}$  then
      return
    end if
  end for
end function

```

from RRT* [18], we do not perform the rewiring of the tree when a new node is inserted, what would not be straight forward due to wind. This fact may lead our approach to generate sub-optimal paths, since rewiring is necessary to prove the asymptotically optimality of RRT*. Our motion planner is shown in Alg. 1, and its functions are described in the sequence.

1) *Sampling*: The *Sample* function randomly chooses a configuration $\mathbf{x}_{rand} \in \mathbb{C}$ from the configuration space and creates a vertex v_{rand} with it.

2) *Closest Neighbor*: Given a vertex v_{rand} and the tree $\tau(V, E)$, the *Nearest* function returns the nearest vertex $v_{nearest} \in V$ according to a distance function. At this point a simple Euclidean metric is used to select $v_{nearest}$, in order to keep a low computational load.

3) *Steering*: The *ApproxSteer* function creates a new vertex v_{new} in the direction given by the nearest vertex and the vertex sampled randomly. This new vertex is created at a distance given by the step size d . The heading angle is set as aligned with this direction.

4) *Near Neighbors*: Given the new vertex v_{new} and the tree $\tau(V, E)$, the *Near* function returns a set the vertices $V_{near} \in V$ that are at a certain distance l from the new vertex. The Euclidean distance is used as a metric to obtain this set. The threshold l is calculated using the optimal formulation proposed in [16].

5) *Best Parent*: The function *BestParent*, shown in Alg. 2, selects the best parent vertex from the set of near vertices V_{near} by comparing the costs of steering from each of them to the new vertex, v_{new} , using the *DubinsSteer* function (Alg. 3). Fig. 5 illustrates how the selection of the best parent process works.

6) *Steering With Dubins*: The local planner *DubinsSteer*, shown in Alg. 3, calculates a path connecting a given vertex v_{near} to v_{new} using an extended 3D version of the Dubins' paths. As described in [19] we consider that the airspeed, v_a , is constant, and that the roll angle ϕ can only assume three values $\{\phi_{min}, 0, \phi_{max}\}$ (in other words, the aircraft

Algorithm 2 Choosing the best parent for a new vertex

```

function  $v_{min}, v_{new} = \text{BESTPARENT}(V_{near}, v_{nrst}, v_{new})$ 
   $v_{new}, c_{min} \leftarrow \text{DubinsSteer}(v_{nrst}, v_{new})$ 
  for  $v_{near} \in V_{near}$  do
     $v'_{new}, c' \leftarrow \text{DubinsSteer}(v_{near}, v_{new})$ 
    if  $c' < c_{min}$  then
       $v_{new} \leftarrow v'_{new}$ 
       $c_{min} \leftarrow c'$ 
    end if
  end for
end function
  
```

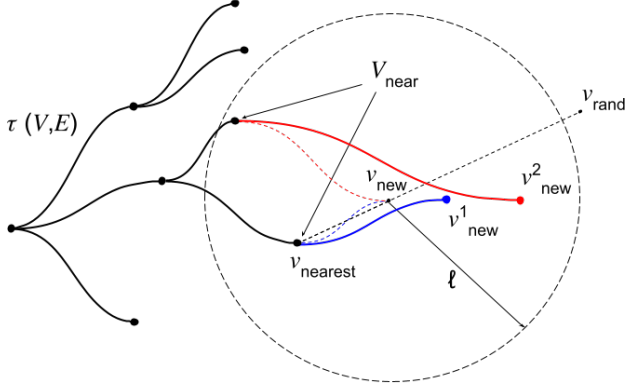


Fig. 5: The new vertex v_{new} is connected using Dubins' Airplane to all vertices in set V_{near} (dashed colored curves). These curves are deformed due to the effect of the wind (solid colored curves). The cost for each of the wind-deformed curves is calculated and ranked. The vertex v_{new}^i with lowest cost is added to the tree $\tau(V, E)$.

is capable of turning in maximum rate or follow a straight heading angle), and the flight path angle, γ , can assume any value within its limits $[\gamma_{min}, \gamma_{max}]$. Therefore, DubinsPath finds the sequence of inputs $u = [v_a, \gamma, \phi]^T$ that takes the system from v_{near} to v_{new} in the wind reference frame, i.e., without considering the effect of the wind.

Based on the method presented in [11], the function DeformTrajectory (Alg. 4) discretizes the Dubins' path at regular time intervals Δt . Then the loop deforms the trajectory from the wind reference frame to the ground frame by adding the integrated wind drift at each time step using a WindField function to obtain a wind vector for each ground-relative position. This process is illustrated in Fig. 6.

The new trajectory, now in the ground reference frame, is used to calculate the required thrust at every instant (RequiredThrust) using the formulation presented in Sect. II. With the necessary thrust and the ground-relative trajectory, the cost for this potential edge is calculated, using the Cost function, explained next. Fig. 5 shows how this step is used in our algorithm.

7) *Energy-Based Cost Function*: In our planner we are proposing an energy-based Cost function that takes into account the energy expenditure due to the propulsive system, and a heuristic to account for the changes in potential energy

Algorithm 3 Steering using Dubins' Airplane and wind

```

function  $v_{new}, c_{min} = \text{DUBINSSTEER}(v_{near}, v_{new})$ 
   $\sigma \leftarrow \text{DubinsPath}(v_{near}, v_{new})$ 
   $S_{wind} \leftarrow \text{DeformTrajectory}(\sigma, N, v_a)$ 
   $v_{new} \leftarrow S_{wind}(\text{end})$ 
   $T \leftarrow \text{RequiredThrust}(S_{wind})$ 
   $c_{min} \leftarrow \text{Cost}(v_{near}, \sigma_{wind}, T)$ 
end function
  
```

Algorithm 4 Deforming Dubins' trajectory due to wind

```

function  $\sigma_{wind} = \text{DEFORMTRAJECTORY}(\sigma, N, v_a)$ 
   $L \leftarrow \text{GetLength}(\sigma)$ 
   $\Delta t \leftarrow (L/N)/v_a$ 
   $S_{wind} \leftarrow \text{Discretize}(\sigma, \Delta t)$ 
   $D \leftarrow (0, 0, 0)$ 
  for  $i \leftarrow 1, N$  do
     $S_{wind}(i) \leftarrow S_{wind}(i) + D$ 
     $(w_x, w_y, w_z) \leftarrow \text{WindField}(\sigma(i))$ 
     $D \leftarrow D + (w_x, w_y, w_z) \cdot \Delta t$ 
  end for
end function
  
```

and energy accumulation due to charging of the batteries with the solar panels. The proposed cost function is given by

$$C = \begin{cases} E_{prop} + E_{pot}^{opp} + E_{solar}^{opp}, & \text{if } b + \Delta b \geq 0 \\ \infty, & \text{if } b + \Delta b < 0 \end{cases} \quad (7)$$

The first component, E_{prop} , is straight-forward, since there is a natural relationship between energy expenditure and cost. The cost is given by the energy obtained by the integration of the instantaneous power required by the propellers:

$$E_{prop} = \int \frac{P_{prop}}{\eta_{prop}\eta_{shaft}} dt = \int \frac{T v_a}{\eta_{prop}\eta_{shaft}} dt, \quad (8)$$

The first component, E_{prop} , is straight-forward, since there is a natural relationship between energy expenditure and cost.

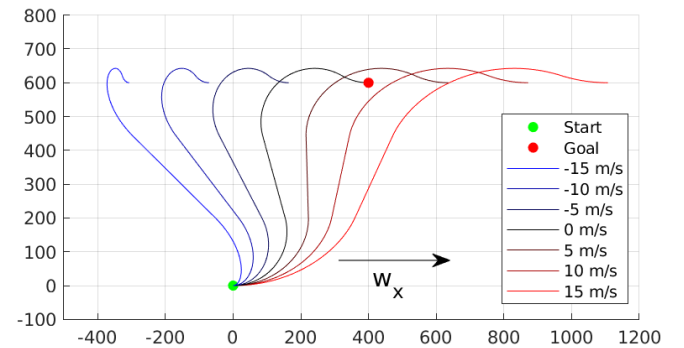


Fig. 6: A trajectory is deformed due to the effect of wind. The black trajectory is obtained by connecting the start and the goal configurations using a Dubins' Airplane path and discretizing this path over a time interval. Using this discretization, we calculate the red and blue trajectories by adding the drift caused by the wind field at each time-step.

The cost is given by the energy obtained by the integration of the instantaneous power required by the propellers:

$$E_{prop} = \int \frac{P_{prop}}{\eta_{prop}\eta_{shaft}} dt = \int \frac{Tv_a}{\eta_{prop}\eta_{shaft}} dt, \quad (9)$$

where the thrust, T , is calculated using (5), and η_{prop} and η_{shaft} are the propellers and shaft efficiencies, respectively.

Including energy gains with solar energy and potential energy is problematic, because, if the energy influx is greater than the energy outflux, negative costs can be encountered, which is unsuitable for optimization. Since there are paths that can maximize the value for both energy components (paths with the maximum altitude), we propose their inclusion as a complement to their respective maximum value. Like in Microeconomics, this can be thought of as opportunity costs: the loss of a prospective gain when one chooses to not use the action that maximizes its benefits [17]. Thus, the opportunity costs for the potential and solar energies are

$$E_{pot}^{opp} = E_{pot}^{max} - E_{pot} = mg(h_{max} - h) \quad \text{and}$$

$$E_{solar}^{opp} = E_{solar}^{max} - E_{solar} = \int (P_{solar}^{max} - P_{solar}) dt, \quad (10)$$

where h_{max} is 70 km and h is the height of the child vertex (local goal), $P_{solar} = I_{solar}\eta_{panels}A_{panels}$ is the solar power accounting for the available solar intensity, I_{solar} , solar panel efficiency, η_{panels} , and solar panel area, A_{panels} . In the atmosphere of Venus, P_{solar}^{max} is the maximum power that the solar panels can absorb, 560 W/m² (reached at the highest altitude, as shown in Fig. 3).

The change in the battery level is calculated using the difference between influx and outflux energies

$$\Delta b = -E_{prop} + E_{solar}. \quad (11)$$

where the thrust, T , is calculated using (5), and η_{prop} and η_{shaft} are the propellers and shaft efficiencies, respectively.

Including energy gains with solar energy and potential energy is problematic, because, if the energy influx is greater than the energy outflux, negative costs can be encountered, which is unsuitable for optimization. Since there are paths that can maximize the value for both energy components (paths with the maximum altitude), we propose their inclusion as a complement to their respective maximum value. Like in Microeconomics, this can be thought of as opportunity costs: the loss of a prospective gain when one chooses to not use the action that maximizes its benefits [17]. Thus, the opportunity costs for the potential and solar energies are

$$E_{pot}^{opp} = E_{pot}^{max} - E_{pot} = mg(h_{max} - h) \quad \text{and}$$

$$E_{solar}^{opp} = E_{solar}^{max} - E_{solar} = \int (P_{solar}^{max} - P_{solar}) dt, \quad (12)$$

where h_{max} is 70 km and h is the height of the child vertex (local goal), $P_{solar} = I_{solar}\eta_{panels}A_{panels}$ is the solar power accounting for the available solar intensity, I_{solar} , solar panel efficiency, η_{panels} , and solar panel area, A_{panels} . In the atmosphere of Venus, P_{solar}^{max} is the maximum power that the solar panels can absorb, 560 W/m² (reached at the highest altitude, as shown in Fig. 3).

The change in the battery level is calculated using the difference between influx and outflux energies

$$\Delta b = -E_{prop} + E_{solar}. \quad (13)$$

8) *Insert Node*: Given the current tree, $\tau(V, E)$, a vertex $v_{min} \in V$, and a new vertex, v_{new} , the *InsertNode* function adds the new vertex, v_{new} , to V and adds an edge (v_{min}, v_{new}) to E . It also assigns the cost of this new edge (local trajectory) and adds this cost to the cost of the parent vertex to create a new total cost associated with the new vertex. Similarly, the child (v_{new}) updates the state of the battery by adding the change in the battery level required to follow the added trajectory.

9) *Termination*: After the new vertex, v_{new} , is added to the tree $\tau(V, E)$, we check if it is in the goal region, specified by d_{min} , which is a hyper-parameter to control how close the solution needs to get from the actual desired position. If the condition is met, the algorithm is terminated and the tree $\tau(V, E)$ is returned. Otherwise, the loop is continued until the maximum number of samples N is reached.

IV. NUMERICAL RESULTS

Our final objective is to obtain a motion planner that is capable of finding optimal trajectories in a planet-sized environment: the Equatorial circumference of Venus is 38 024.6 km (in comparison, the Equatorial circumference of the Earth is 40 030.2 km). However, for the analysis presented in this work, we were more concerned in checking the behavior of our planner and, therefore, smaller environments, in the order of some hundreds of kilometers (Table II), were considered.

In our first example, shown in Fig. 7, we show the relevance of taking into account high-speed winds on the motion planning. In this experiment, we set the airship's airspeed to its maximum value $v_a = 30$ m/s and then used a wind model $\mathbf{w} = [w_x, 0, 0]^T$, varying the values of the longitudinal component w_x . The motion planner run using $N = 1000$ random samples (which are represented by the colored dots in the figure). For each value of w_x , we also compared the effect of two different steering step sizes $d = 10$ km and $d = 50$ km. In Fig. 7(a) we can see a scenario with $w_x = 0$. Since there is no wind, the Dubins' paths are not deformed and the random samples coincide with the vertices of the tree. Furthermore, because $v_a < \|\mathbf{w}\|$, the vehicle is capable of moving in any direction. From Fig. 7(b) to Fig. 7(d), we increase the wind speed and observe that the reachable configurations become limited by a "cone"-like geometry (similar to what is described in [20]). In Fig. 7(b), the wind speed is equal to the airspeed of the vehicle and we can see how the step size can be an important parameter. In an ideal scenario, the vehicle could at most maintain its x coordinate. However, if it chooses to move in the other axes, it is carried by the wind. When a small step size is chosen, the curved parts of the Dubins' trajectories are relatively large compared to its straight part and the cone. If the step size is big, the straight parts are prevalent and the airship is able to move in the y coordinate with low drift in

TABLE II: Configuration Space Limits

Parameters	Values	Parameters	Values
x_{min}	-100 km	x_{max}	100/300 km
y_{min}	-100 km	y_{max}	100 km
z_{min}	55 km	z_{max}	70 km
ψ_{min}	$-\pi$ rad	ψ_{max}	π rad
b_{min}	0 MJ	b_{max}	50 MJ

the x coordinate. As the wind speeds become much larger than the airspeed, the vehicle is not able to counteract the wind speeds that much and the reachable regions is further reduced. This is an important fact for motion planning in Venus. If the distance to our desired goal in the y direction (latitude) is too big and the vehicle is not able to produce speeds to counteract the wind drift, the only possible way to reach it is to circle the planet.

In our second simulation, shown in Fig. 8, we present a solution for a well defined motion planning problem. The start position of the aircraft was set to $\mathbf{p}_{start} = [-100, 0, 55]^T$ km with initial heading set to zero. The goal position was set to $\mathbf{p}_{goal} = [300, 80, 55]^T$ km. The final heading was also set to zero but our planner do not guarantee this heading, since the planner finds paths to a region around the target. The aircraft airspeed was set to be $v_a = 30$ m/s. The 3D wind model used in this setup was again simplified to $\mathbf{w} = [w_x, 0, 0]^T$, but now w_x was computed in function of the altitude of the vehicle, as shown in Fig. 2. The motion planner run with $N = 5000$ random samples and a steering step size of 10 km. The path found by the planner travels the majority of the course on higher altitudes. This is expected since in higher altitudes we find lower air density (i.e. less drag force) and higher availability of solar intensity. A solution was reached at a distance of 3490.9 m from the goal, where the vehicle would arrive with full battery (50 MJ), having traveled a distance of 361.35 km in 4065.0 s. The cost of the path is 221.9 MJ. For the sake of comparison, we connected start and goal configurations with a single Dubins path using an iterative method to account for the wind drift. This solution converged to a position at a distance of 1920.2 m from the goal. The traveled distance would be 360.84 km with total time 3405.4 s. However, the path would not be energetically feasible because the battery would fully discharge before reaching the end ($-E_{prop}^{baseline} + E_{solar}^{baseline} = -598.4$ MJ, which is more than the battery capacity $b_{max} = 50$ MJ).

V. CONCLUSIONS AND FUTURE WORK

This paper presented a motion planning strategy for solar-powered hybrid airships flying in the atmosphere of Venus, where strong winds are present and battery charging is a function of the vehicle's altitude. Our motion planner is able to find low-energy trajectories and is a good first step for a more complete system that will be used in future exploration missions.

Our simulation results show a few limitations of our current implementation. When the aerobot is limited to airspeeds smaller than the wind speed, planning needs to account for

the wrapping nature of the atmospheric environment. If a goal is set against the wind or at higher latitudes, the aircraft needs to go around the planet at least once to reach it. This behavior will be included in our future work. Also, our current implementation does not consider the possibility of motion without thrust (i.e., gliding) when the battery is empty, since we do not expand the search tree using edges that would result in a negative battery level. However, we believe that gliding will be an important feature during the night and we plan to slightly modify the algorithm to account for that. Additionally, our current simulations consider the wind field as time-invariant and mostly unidirectional. In the future we want to consider a more complete model of Venus atmospheric wind. We also want to include local measurements of the wind and include multiple vehicles in coordinated missions.

REFERENCES

- [1] A. T. Basilevsky and J. W. Head, "The surface of Venus," *Reports on Progress in Physics*, vol. 66, no. 10, pp. 1699–1734, Sept. 2003, publisher: IOP Publishing. [Online]. Available: <https://doi.org/10.1088/0034-4885/66/10/r04>
- [2] M. Marov, "Results of Venus Missions," *Annual Review of astronomy and astrophysics*, vol. 16, no. 1, pp. 141–169, 1978.
- [3] G. Landis, A. Colozza, and C. LaMarre, "Atmospheric flight on Venus," in *40th AIAA Aerospace Sciences Meeting & Exhibit*. Reno,NV,U.S.A.: American Institute of Aeronautics and Astronautics, Jan. 2002. [Online]. Available: <https://arc.aiaa.org/doi/10.2514/6.2002-819>
- [4] James A. Cutts, Larry H. Matthies, and Thomas W. Thompson, "Aerial Platforms for the Scientific Exploration of Venus," NASA Jet Propulsion Laboratory, Tech. Rep., 2018. [Online]. Available: https://solarsystem.nasa.gov/system/downloadable_items/2693_Venus_Aerial_Platforms_Final_Report_Summary_Report_10_25_2018.pdf
- [5] G. A. Landis, "Exploring Venus by solar airplane," in *AIP Conference Proceedings*, vol. 552. Albuquerque, New Mexico: AIP, 2001, pp. 16–18, iSSN: 0094243X. [Online]. Available: <http://aip.scitation.org/doi/abs/10.1063/1.1357898>
- [6] Z. Rubin, A. Aboelezz, B. Herkenhoff, and M. Hassanalain, "Drones for Venus Exploration: Energy Harvesting Mechanisms and Thermal-based Flight Control," in *AIAA Scitech 2021 Forum*. American Institute of Aeronautics and Astronautics, 2021. [Online]. Available: <https://arc.aiaa.org/doi/abs/10.2514/6.2021-1537>
- [7] E. Z. Noe Dobrea, J. Freeman, A. R. Gibson, D. Hall, L. Lemke, B. Pham, and B. T. Schiltgen, "Exploring aircraft and mission profile designs for long-duration flight in the Venusian atmosphere," in *AIAA Scitech 2020 Forum*. Orlando, FL: American Institute of Aeronautics and Astronautics, Jan. 2020. [Online]. Available: <https://arc.aiaa.org/doi/10.2514/6.2020-2017>
- [8] R. Polidan, G. Lee, D. Sokol, K. Griffin, and L. Bolisay, "Venus Atmospheric Maneuverable Platform (VAMP)," in *Workshop on Venus Exploration Targets*, vol. 1781, May 2014, p. 6011, conference Name: ADS Bibcode: 2014LPICo1781.6011P. [Online]. Available: <https://ui.adsabs.harvard.edu/abs/2014LPICo1781.6011P>
- [9] A. Sánchez-Lavega, S. Lebonnois, T. Imamura, P. Read, and D. Luz, "The Atmospheric Dynamics of Venus," *Space Science Reviews*, vol. 212, pp. 1541–1616, Nov. 2017, aDS Bibcode: 2017SSRv..212.1541S. [Online]. Available: <https://ui.adsabs.harvard.edu/abs/2017SSRv..212.1541S>
- [10] G. A. Landis and E. Haag, "Analysis of Solar Cell Efficiency for Venus Atmosphere and Surface Missions," in *11th International Energy Conversion Engineering Conference*, ser. Joint Propulsion Conferences. American Institute of Aeronautics and Astronautics, July 2013. [Online]. Available: <https://arc.aiaa.org/doi/10.2514/6.2013-4028>
- [11] P. Oettershagen, F. Achermann, B. Müller, D. Schneider, and R. Siegwart, "Towards Fully Environment-Aware UAVs: Real-Time Path Planning with Online 3D Wind Field Prediction in Complex Terrain," *arXiv:1712.03608 [cs]*, Dec. 2017, arXiv: 1712.03608. [Online]. Available: <http://arxiv.org/abs/1712.03608>

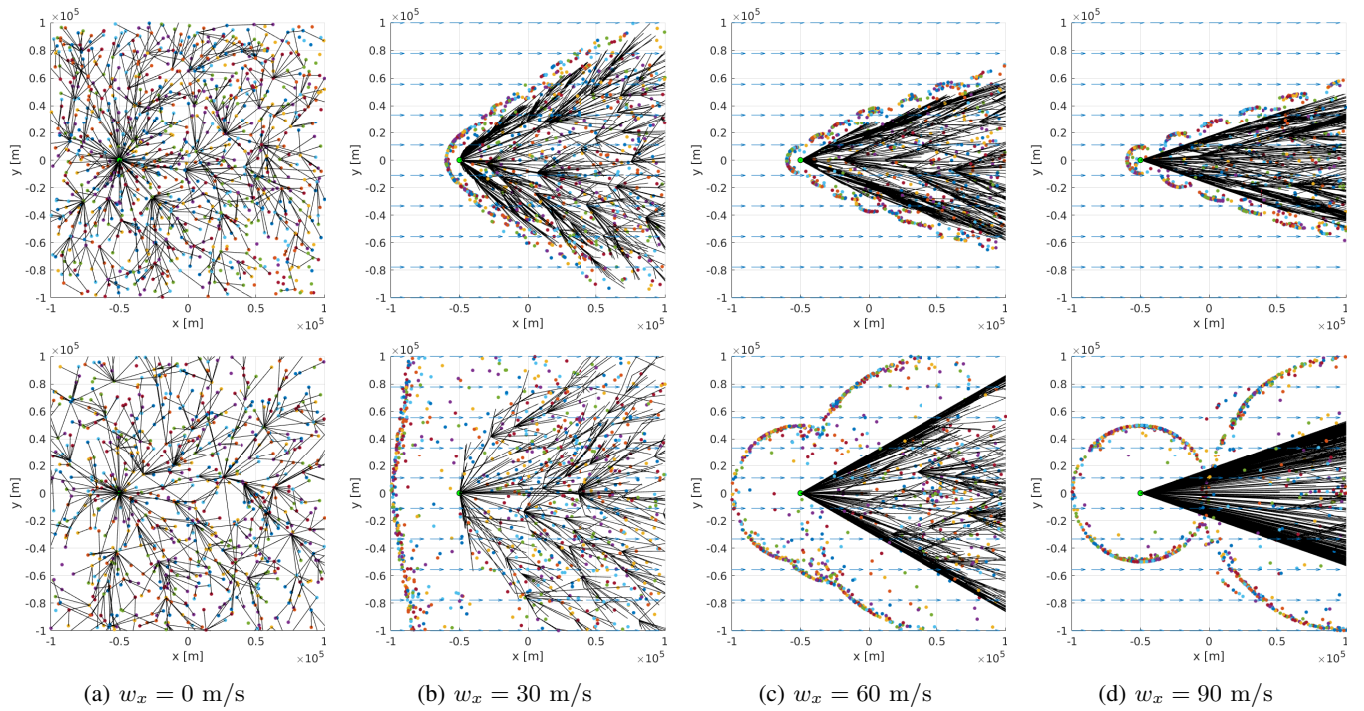
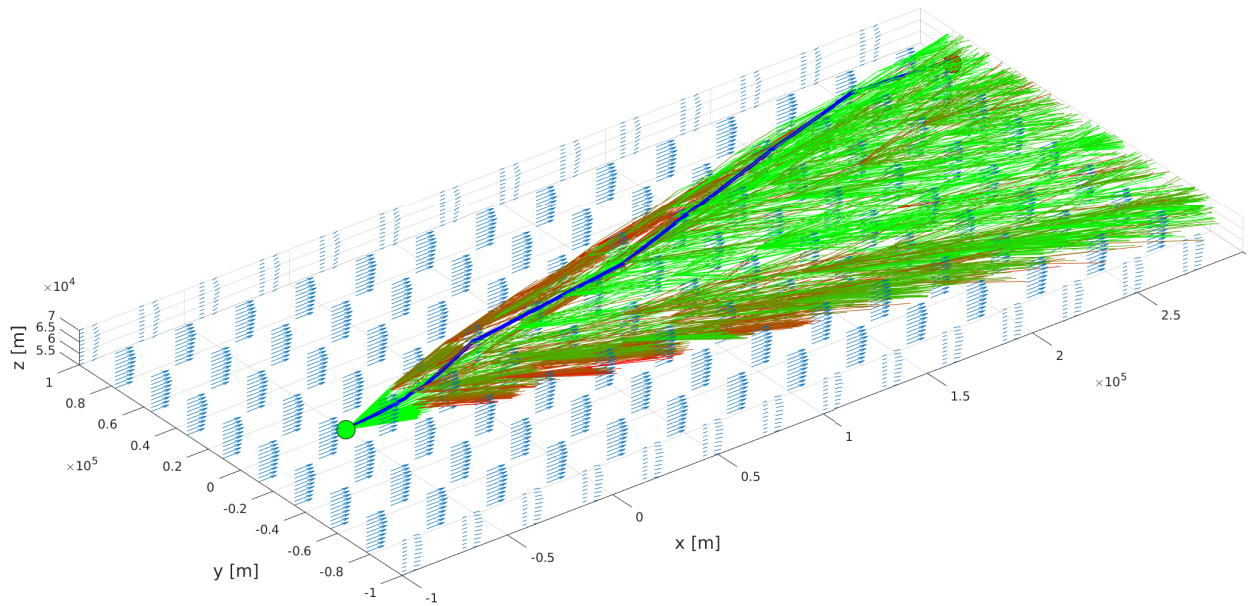
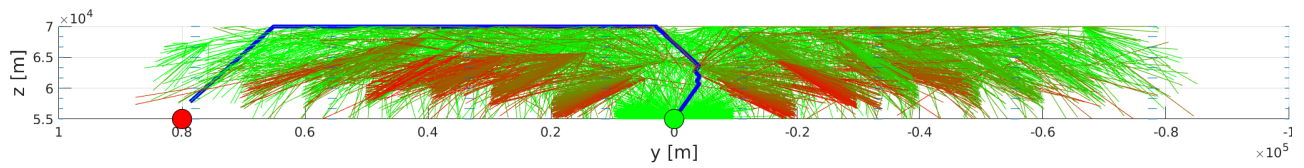


Fig. 7: Effect of the winds in the planning tree. Airspeed $v_a = 30$ m/s. Steering step-size $d = 10$ km in the top figures and $d = 50$ km in the bottom figures.

- [12] H. Chitsaz and S. M. LaValle, "Time-optimal paths for a Dubins airplane," in *2007 46th IEEE Conference on Decision and Control*, Dec. 2007, pp. 2379–2384, iSSN: 0191-2216.
- [13] J. Ware and N. Roy, "An analysis of wind field estimation and exploitation for quadrotor flight in the urban canopy layer," in *2016 IEEE International Conference on Robotics and Automation (ICRA)*, May 2016, pp. 1507–1514.
- [14] J. W. Langelaan, "Tree-based trajectory planning to exploit atmospheric energy," in *2008 American Control Conference*, June 2008, pp. 2328–2333, iSSN: 2378-5861.
- [15] A. Chakrabarty and J. Langelaan, "UAV flight path planning in time varying complex wind-fields," in *2013 American Control Conference*, June 2013, pp. 2568–2574, iSSN: 2378-5861.
- [16] S. Karaman and E. Frazzoli, "Sampling-based Algorithms for Optimal Motion Planning," *arXiv:1105.1186 [cs]*, May 2011, arXiv: 1105.1186. [Online]. Available: <http://arxiv.org/abs/1105.1186>
- [17] J. M. Buchanan, "Opportunity Cost," in *The World of Economics*, ser. The New Palgrave, J. Eatwell, M. Milgate, and P. Newman, Eds. London: Palgrave Macmillan UK, 1991, pp. 520–525. [Online]. Available: https://doi.org/10.1007/978-1-349-21315-3_69
- [18] S. Karaman, M. R. Walter, A. Perez, E. Frazzoli, and S. Teller, "Anytime Motion Planning using the RRT*," in *2011 IEEE International Conference on Robotics and Automation*. Shanghai, China: IEEE, May 2011, pp. 1478–1483. [Online]. Available: <http://ieeexplore.ieee.org/document/5980479/>
- [19] M. Owen, R. W. Beard, and T. W. McLain, "Implementing Dubins Airplane Paths on Fixed-Wing UAVs*," in *Handbook of Unmanned Aerial Vehicles*, K. P. Valavanis and G. J. Vachtsevanos, Eds. Dordrecht: Springer Netherlands, 2015, pp. 1677–1701. [Online]. Available: https://doi.org/10.1007/978-90-481-9707-1_120
- [20] M. Soullignac, "Feasible and Optimal Path Planning in Strong Current Fields," *IEEE Transactions on Robotics*, vol. 27, no. 1, pp. 89–98, Feb. 2011.



(a) 3D view



(b) YZ view

Fig. 8: Motion planning for airship flying in the atmosphere of Venus with start and goal positions given by the green circle and red circles. A tree of kinematically feasible trajectories is created considering the effect of the wind drift. Higher altitudes are preferred by the solution trajectory (in blue) because at this altitudes the aircraft finds less air resistance and highest solar energy for charging its batteries. The colored edges on the tree show the battery capacity after the vehicle follows the edge: the color changes from green to red according to the battery level (green is full and red is empty).